IEEE Photonics Journal
An IEEE Photonics Society Publication

Open Access

Full-Field Swept Source Master-Slave Optical Coherence Tomography

Volume 7, Number 4, August 2015

Jingyu Wang
Adrian Bradu
George Dobre
Adrian Podoleanu

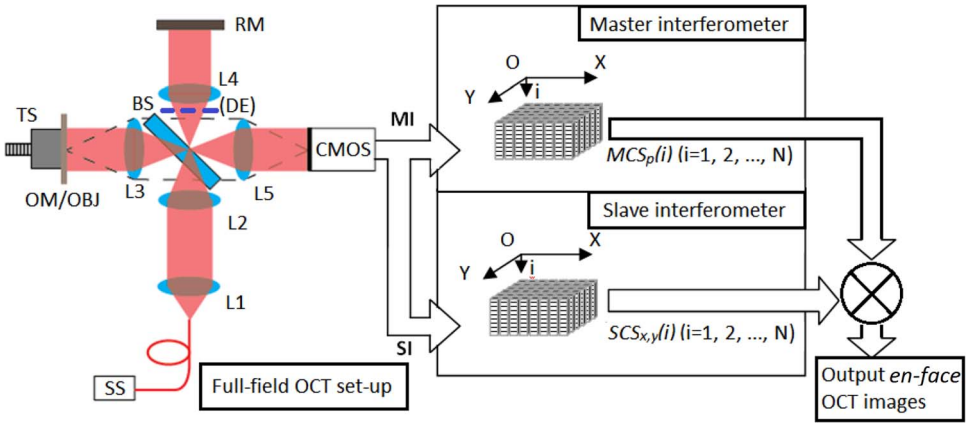

DOI: 10.1109/JPHOT.2015.2461571
1943-0655 © 2015 IEEE

IEEE photonics SOCIETY

IEEE

Full-Field Swept Source Master-Slave Optical Coherence Tomography

Jingyu Wang, Adrian Bradu, George Dobre, and Adrian Podoleanu

Applied Optics Group, School of Physical Sciences, University of Kent, Kent CT2 7NH, U.K.

DOI: 10.1109/JPHOT.2015.2461571

Manuscript received July 22, 2015; accepted July 24, 2015. Date of publication July 28, 2015; date of current version August 12, 2015. This work was supported by the European Research Council under the European Union's Seventh Framework Programme, Advanced Grant "COGATIMABIO," No. 249889. The work of A. Podoleanu was also supported by the National Institute for Health Research (NIHR) Biomedical Research Centre at Moorfields Eye Hospital National Health System (NHS) Foundation Trust and University College London (UCL) Institute of Ophthalmology. Corresponding author: J. Wang (e-mail: j.y.wang@kent.ac.uk).

Abstract: We apply the principle of master-slave (MS) interferometry to a full-field swept source optical coherence tomography (OCT) setup equipped with a fast 2-D camera. MS interferometry does not involve Fourier transformations and, therefore, eliminates the need for spectrum data resampling required by the conventional spectral domain OCT. Using this method in a full-field OCT setup, *en face* images are acquired in vivo from finger skin, Drosophila melanogaster larvae, and pupae, with no spectrum resampling and no mechanical scanning. The signal processing is based on a comparison operation of the shapes of channeled spectra for each camera pixel, with a set of reference signals (masks). In this way, *en face* OCT images can be obtained with no need for the volumetric assembly and software cutting the *en face* images from an image volume, which are required by the conventional spectral domain OCT method. We demonstrate that the sensitivity and axial resolution of the MS method in a full-field swept source OCT setup are similar to the values obtained using the conventional Fourier-transformation-based swept source OCT method in a full-field setup. Multiple *en face* images can be produced in parallel by using multiple stored shapes of channeled spectra for the depths of interest. The full-field MS-OCT method presented here opens the possibility of parallel processing for all image points in a 3-D volume of the object.

Index Terms: Optical coherence tomography, interferometric imaging, parallel processing.

1. Introduction

Spectral domain optical coherence tomography (SD-OCT) is an established technique that produces cross-section images (B-scans) with high axial resolution and high sensitivity [1]. Current SD-OCT systems, using either a spectrometer-based approach, (Sp-OCT) [2] or a swept-source OCT (SS-OCT) approach [3], produce an electrical signal proportional to the oscillation of the modulated (channeled) optical spectrum at the interferometer output, due to interference. Performing a Fourier transformation (FT) of the electrical signal, an A-scan (reflectivity profile in depth) is obtained. In what follows, we refer to both such methods as SD-OCT methods, although in some prior reports, they were both referred to as either spectral-domain or Fourier-domain OCT methods. B-scan images are assembled from A-scans acquired for adjacent lateral positions from the target medium. However, some biomedical applications require *en face* OCT images (C-scans) [4] to be presented alone or beside the B-scan images, usually for better

visualization of microstructures, as the additional information conveyed by the *en face* images can enhance the physicians' understanding of the pathology. For example, spatial registration of the cross-sectional image to the *en face* image is desired in ophthalmology for monitoring data quality, locating pathology, increasing reproducibility and detecting eye movements [5], [6]. In SD-OCT, *en face* images are reconstructed from a 3-D rendering after a whole high-density volumetric data is acquired, normally via a post-acquisition process. In most cases, a collection of A-scan signals from 2-D transverse coordinates is employed to build the volume. Then, by sectioning the volume at a certain depth position, an *en face* image is generated. The time to assemble an accurate volume of data includes the acquisition time of channeled spectra plus the time of their post-processing, which usually involves spectrum re-sampling [7], digital windowing or spectral shaping [8] and sometimes zero-padding [9] before FT. Repeating all these processing steps, which have to be sequentially executed, requires considerable time. Thus, conventional SD-OCT set-ups are slow and computationally inefficient in generating *en face* (C-scan) images. Spectrum re-sampling is usually required because the electrical signals delivered by either a spectrometer in Sp-OCT or by a photo-detector in SS-OCT are usually nonlinear in respect to the wavenumber, k. There are two main sources of non-linearity in k: the non-linearity of either the spectrometer in Sp-OCT or the non-linearity in sweeping the frequency of the light source in SS/OCT, to which the systematic dispersion mismatch in the interferometer should be added. Several hardware and software solutions have been devised to attain linearity. Hardware solutions include using a prism to compensate for the dispersion mismatch in Sp-OCT [10] or using a supplementary clock block and a fast photo-detector to provide frequency calibration in SS-OCT [11], [12]. Software techniques usually involve linearizing k to its unwrapped phase [13]. All these solutions require either additional equipment or customized devices or considerable processing time. Additionally, these methods themselves bring some limitations such as in SS-OCT, where the clock limits the maximum axial range. A different method, Master-Slave interferometry [14]–[16] was proposed with two advantages in one package: a) when applied to OCT, it is capable of producing an *en face* OCT image directly without having to first generate a volume of A-scans and then cutting it transversally (in fact FT-based A-scans are totally avoided) and b) the MS interferometry does not need any spectrum re-sampling. The original MS method uses an interferometer set-up operating in two modes, in a master interferometer (MI) mode and in a slave interferometer (SI) mode. In the MI mode, a master channeled spectrum (MCS) is acquired from the interferometer by using a single reflector in the object arm placed at a known optical path difference value, OPD_p. In the SI mode, the single reflector is replaced by the object of interest and a slave channeled spectrum (SCS) is acquired. Rather than analyzing the frequency components of the channeled spectrum so obtained, as done in conventional SD-OCT, the MS-OCT method employs a comparison block that compares the similarity of the two channeled spectrum shapes, MCS and SCS acquired in the two modes (MI and SI respectively). The comparison block employs a modified correlation-based algorithm. The higher the similarity of the channeled spectra shapes, the larger the value at the output of the comparison block. In this way, an *en face* image is produced from the same axial position as determined by the optical path difference OPD_p used to acquire the MCS. The brightness of each lateral pixel in the *en face* image so created is proportional to the degree of similarity of the two channeled spectra correlated.

Due to its principle of operation, the MS interferometry method presents some unique properties compared to conventional SD-OCT. In SD-OCT, the signal processing is based on FT, in which case, all data points along a longitudinal direction (an A-scan) are delivered at once, whereas the MS interferometry delivers the strength of interference at a single axial location determined by OPD_p, similar to time-domain OCT. However, because the signal is handled by a spectral domain interferometry method, the sensitivity typical to SD-OCT is still retained. As already stated, the MS interferometry method does not need spectrum re-sampling. A simple explanation for the tolerance to chirped channeled spectra consists in the fact that both the MCS from the test mirror in the MI mode and the SCS from the object in the SI mode are affected by the same chirping. Therefore, the comparison operation of the MCS and SCS shapes leads to a

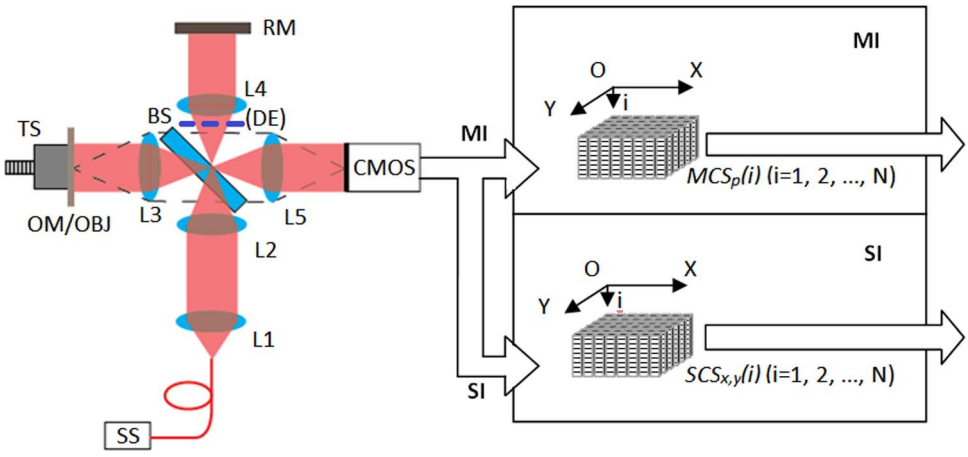

Fig. 1. (a) Schematic of the full-field swept source OCT Setup: SS, swept source, consisting of a Superlum swept source together with an optical amplifier; L1 to L5, achromatic doublet; BS, plate beam splitter; OBJ, object under investigation; OM and RM, two silver coated mirrors used as object mirror and reference mirror, respectively; TS, translation stage; DE, dispersion element, consisting in a glass slab used to demonstrate the dispersion tolerance of the MS-OCT method; CMOS, Photron Fastcam SA3 high-speed CMOS camera. (b) Data stored in the camera memory in the MI and SI modes of operation.

result independent of chirping. In other words, the MS method is immune to the channeled spectrum chirp, irrespective of its origins, wavenumber tuning in swept source based SD-OCT, spectrometer nonlinearity in spectrometer based SD-OCT, or dispersion mismatch in the interferometer.

The operation of the MS method is different from that reported in [17], where the amplitude of signals from a single depth while tuning the swept source are obtained by mixing the photodetected signal with a reference signal of a particular frequency delivered by a local oscillator. Although this method does not require Fourier transformation, a *k*-linear swept source is necessary because the reference frequency provided by the local oscillator does not include the chirping information of the OCT system.

Previous MS interferometry reports [14]–[16] still require transversal scanning of probing beams to obtain data of *en face* OCT images. In this paper, we describe an implementation of the MS method in a full-field OCT [18] set-up, which eliminates any mechanical scanning. In order to compare this method with the conventional FT based method [19], [20], the same optical setup is also used to deliver A-scans by applying a fast Fourier transformation (FFT) to the channeled spectrum acquired. To distinguish between the two cases, we use the notation MS-OCT to refer to the set-up employing MS interferometry, and FT-OCT to refer to the set-up employing FFT. Both cases involve a full-field (FF) set-up and a swept source OCT principle, however in order to keep the notation short, the acronyms FF and SS are dropped.

2. Methods and Experimental Set-Up

The full-field swept source OCT setup is built as illustrated in Fig. 1(a). The setup is identical to a conventional full-field OCT. A Superlum swept source SS (BS840-02, wavelength tuning range 828–873 nm, linewidth 0.05 nm, maximum tuning rate 2 kHz) is used as a light source, delivering 3 mW. For imaging scattering samples, the power was further amplified by a booster, SOA-840 (Superlum, Cork, Ireland), delivering 25 mW. Light is collimated by an achromatic doublet L1 $(f = 50$ mm$)$ and directed towards a Michelson interferometer, creating an incident optical beam with a diameter of $\sim$6 mm FWHM. Another achromatic doublet L2 $(f = 150$ mm$)$ is used to focus the beam. The light beam is split by a 50-50 plate non-polarised beam splitter BS into two beams: an object beam towards the object OBJ and a reference beam towards a reference mirror RM. An object mirror OM is used in the MI mode, which is replaced subsequently in the SI mode, with the target object OBJ. Both beams are collimated by two identical achromatic doublets L3 and L4 (both have $f = 25.6$ mm, N.A. $= 0.16$). L2, L3, and L4, together produce

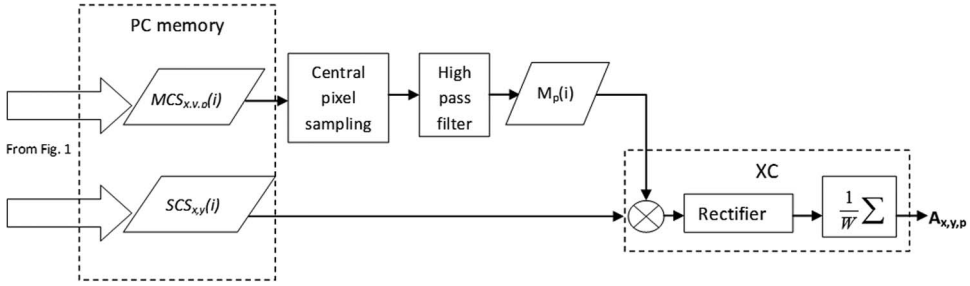

Fig. 2. Flowchart of the MS-OCT algorithm performed by the comparison block XC in the second stage imaging (SI mode of operation).

flood-illumination of the OBJ and RM. The illumination beams on the OM and RM are both $\sim$1 mm (FWHM) in diameter. The two beams are reflected by OM/OBJ and RM respectively back to the BS along the reverse of their outgoing paths. The two return beams recombine at BS. The transmitted object signal and the reflected reference signal are guided to a high-speed camera, Photron FASTCAM SA3 (Photron, CA) via an achromatic doublet, L5 $(f = 150$ mm$)$. The camera is set to acquire images of X pixels along the horizontal direction (x coordinate), and Y pixels along the vertical direction (y coordinate) and stores the data on its onboard memory in the process of image sequence acquisition. After the acquisition phase is finished, the image data is downloaded to the PC via a gigabit Ethernet (GigE) connection. L5, together with L3, ensure that the surface of the CMOS sensor is conjugated to the imaging plane at OM/OBJ. The acquisition on the CMOS is synchronized with the beginning of the SS sweep. An optional component, (DE), a slab of glass tube that is 25.4 mm thick is used in the reference path to introduce dispersion with the goal to demonstrate the tolerance of the MS method to dispersion. This is shown in dashed line, as it is used to obtain the graphs in Fig. 4(d) only.

The setup in Fig. 1(a) is used in two steps. In the first step, the interferometer is used as a Master Interferometer in the MI mode. An object mirror (OM) is aligned to be perpendicular to the incoming optical beam and is placed at an axial position corresponding to an OPD value OPD_p. Then the SS is swept and the synchronized CMOS continuously records 2-D images that are stored in the camera memory. Considering that N frames are acquired during each sweep, these correspond to N wavenumber values within the tuning range of the swept source. After each sweep, N of $MCS_{x,y,p}(i)$ images for $i = 1, 2, \ldots, N$ are obtained that are stored within the camera memory, then the set of N $MCS_{x,y,p}(i)$ images is transferred to the PC, as shown in Fig. 2, where signal is retained from a pixel in the center of images only. After being passed through a high-pass filter (HPF), the signal is stored in the PC memory as a Mask $M_p(i)$, which represents an electrical signal that consists of N samples, a sample for each wavenumber i. Repeating this process for P positions of the OM, at P OPD values $\text{OPD}_1, \text{OPD}_2, \ldots, \text{OPD}_p, \ldots, \text{OPD}_P$, P masks $M_1(i), M_2(i), \ldots, M_p(i), \ldots, M_P(i)$ are obtained and stored in the computer memory to be used in the second stage: the SI mode. Fine tuning of OPD_p is achieved by using a motorized linear translation stage, TS in Fig. 1(a), equipped with a DC-servo motor, UE16CC (Newport Corp., Irvine, CA) which moves the OM axially. The motor allows axial motion with a resolution of 55 μm.

In the second step, i.e., the SI mode, the interferometer is used as a slave interferometer, OM is replaced by the imaging target, OBJ, placed in the focus of L3 and N images are acquired while tuning the swept source. We refer to these images as slave channeled spectra, $\text{SCS}_{x,y}(i)$. They are initially stored in the camera memory, illustrated in Fig. 1(b), and then transferred to the PC (see Fig. 2). The hardware acquisition is similar to that in the MI mode except that instead of retaining the signal from a single pixel as a mask, the entire 2-D array of channeled spectra data are acquired, each at a camera pixel (x, y). Finally, as shown in Fig. 2, the $SCS_{x,y}(i)$ together with the mask $M_p(i)$ are read from the PC memory and are passed to the two inputs of a comparator block, XC. The comparator XC is at the core of the MS-OCT algorithm [14]. This block

compares the set of masks $M_p(i)$ as channeled spectra acquired from the OM (modified according to the processing shown in Fig. 2), with the $SCS_{x,y}(i)$, which is obtained from the OBJ.

The signal processing of the acquired channeled spectrum $SCS_{x,y}(i)$ for each pixel (x, y) involves three steps, as shown in Fig. 2.

1) The signal with $i = 0, 1, 2, 3 \ldots, N-1$ is cross-correlated with a mask $M_p(i)$ with $i = 0, 1, 2, 3 \ldots, N-1$, which can be written as

$$\mathrm{Corr}_{x,y,p}(j) = \sum_{i=0}^{N-1} \mathrm{SCS}_{x,y}(i) M_p(i+j), \qquad (j = -N+1, \ldots, -1, 0, 1, \ldots, N-1) \tag{1}$$

   where $SCS_{x,y}(i)$ and $M_p(i)$ are zero if $i < 0$ and $i \geq N$. There are N images in each of the $M_p(i)$ and $SCS_{x,y}(i)$ sets. The correlation product extends over $2N-1$ lag values where the amplitude at $j = 0$ represents the correlation value for a wavenumber lag equal to zero and quantifies the similarity of the two shapes.
2) The HP filter output is then rectified.
3) Ultimately, an average is calculated over a small interval of lag values $2W+1$, around the center point, $j = 0$, to make the output tolerant to potential phase changes in the channeled spectrum from the time the MCS was collected. The window value W is an integer number much smaller than N. The inevitable phase change may produce a small shift of the peak position in the correlation output and therefore an average is needed. The window averaged signal produces the reflectivity value $A_{x,y,p}$ for the scattering center placed at the lateral pixel (x, y) and at the axial position where the OPD is used to store the mask M_p.

The three-step algorithm can be written in a single formula as

$$A_{x,y,p} = \frac{1}{W} \sum_{j=-W}^{W} \left| \left[\sum_{i=0}^{N-1} SCS_{x,y}(i) M_p(i+j) \right] \right|. \tag{2}$$

Repeating this procedure for each (x, y) pixel in the $SCS_{x,y}(i)$ images, i.e., for $X \times Y$ times, a complete *en face* image is obtained. Correlating $SCS_{x,y}(i)$ with masks M_p, acquired from P different OPD_p values leads to P *en face* OCT images. The XC algorithm is implemented in Matlab.

To compare the MS-OCT method with the conventional SD-OCT, for all experiments to follow, the same data $SCS_{x,y}(i)$ for all $X \times Y$ values were also used to produce *en face* images based on the conventional full-field swept-source OCT method [19]. For this purpose, an A-scan is obtained by applying a FFT to the data at each (x, y) pixel in the set of images $SCS_{x,y}(i)$, $(i = 1, 2, \ldots, N)$. The output is a symmetric signal of which only half is retained, whose amplitude as a function of depth represents an A-scan. For benchmarking purposes, the SCS data were re-sampled using a cubic spline interpolation before the FFT in order to organize the data linearly to wavenumber. The $X \times Y$ A-scans are arranged in a 3-D data volume, with an A-scan for each pixel (x, y). Alternatively, the data so organized can be considered as an assembly of a number $N/2$ of *en face* OCT images of $X \times Y$ size. For a wavelength tuning range of $\Delta\lambda = 45$ nm and $N = 500$ steps, the equivalent spectral resolution becomes $\delta\lambda = 90$ pm. This values determines an imaging axial range of $\Delta z = \lambda_o^2 / 4n\delta\lambda = 2$ mm measured in air [21]. For $N/2 = 250$ *en face* images, the axial interval between adjacent images results as 8 μm. To retrieve *en face* images at the depths of interest, the FT-OCT method requires completion of signal processing of the whole volume of $(N \times X \times Y)$ of data. Only then, an *en face* image can be cut from the volume.

The CMOS camera is capable of delivering up to 1000 frames per second (fps) at full resolution ($X = 1024$, $Y = 1024$), i.e., 1 ms integration time per frame. For *in vivo* imaging, in order to minimize the movement effects, an integration time as short as possible is needed. Therefore, the image size is reduced to 512 $\times$ 128 pixels, which allows a higher rate of 10 000 frames per second, i.e., an integration time for each shot of about 100 μs. For 500 images, this requires an

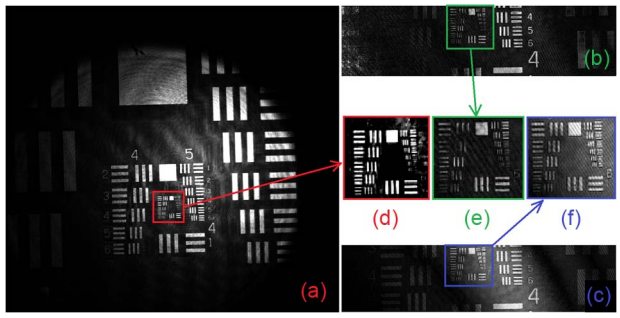

Fig. 3. Images of USAF-1951. (a) Direct view from camera, no reference beam. (b) FT-OCT. (c) MS-OCT. Zoomed images around group 7 bars in (a)–(c) are displayed in (d)–(f), respectively.

acquisition time of 50 ms. Therefore, the SS is tuned at a repetition frequency of 20 Hz. In this case, the camera produces an equivalent data rate of 7.86 Gigabit per second.

We processed the same image sequences obtained from the set-up through both MS-OCT and FT-OCT protocols and compared the results in several respects, including spatial resolution, sensitivity and signal processing speed. In order to be able to compare the two methods directly at different depths from the OBJ, for MS-OCT, 130 MCSs were recorded and used in the following experiments. Since the depth increment of image sequence in FT-OCT is $\sim$8 μm, for MS-OCT, 125 MCSs are acquired from depths of $z = 8$ μm to $z = 1$ mm with a 8 μm increment (measured in air). 5 more MCSs are acquired from $z = 1.2$ mm to $z = 2.0$ mm with a 200 μm increment to evaluate comparatively the decay of sensitivity over an extended axial range. The 5 MCSs from $z = 1.2$ mm to $z = 2.0$ mm are not employed in constructing any images. It is also known that penetration depth of a full-field setup in highly-scattering biomedical samples is generally limited to no more than 1 mm and therefore there is no intention to build images from such large depths using either the FT-OCT and MS-OCT method. The number of Master channeled spectra can be selected flexibly according to the required precision along the axial coordinate. However, the separation of OPD_p of consecutive MCSs should not be smaller than the axial resolution, whose value is quantified in the following. For FT-OCT method, as linearization is required, the re-sampling index was retrieved using a channeled spectrum obtained from a mirror placed at $z = 800$ μm.

3. Resolutions

An USAF-1951 resolution chart was used as OBJ placed at an axial position, $z = 616$ μm measured from OPD $= 0$. Output images for both FT-OCT and MS-OCT methods, as shown in Fig. 3(b) and (c) respectively, are presented next to the direct image from the camera with no processing, as shown in Fig. 3(a). The direct image was obtained by blocking the reference path. The group 7 bars in Fig. 3(a)–(c) are zoomed in and displayed in Fig. 3(d)–(f), respectively. All three zoomed images look similar in both contrast and resolution. The lateral resolution measured from the chart is 7 μm (group 7 element 2) for both FT-OCT and MS-OCT methods, as shown in Fig. 3(e) and (f), respectively. The field of view (FOV) of the CMOS is 1.45 mm $\times$ 0.363 mm. The illuminated FOV of the whole camera sensor can potentially reach 2 mm $\times$ 2 mm, allowed by a slower frame rate and slower wavelength tuning, in case the imaging target is stationary.

To evaluate the axial resolution of the MS-OCT method, a mirror, used as the object OBJ is placed at an axial position $z = 792$ μm. Using a neutral density filter, the signal from the mirror is attenuated by 40 dB. The acquired SCS is correlated with 125 MCSs acquired in the MI mode to obtain 125 values of an A-scan profile at 125 different axial positions. The A-scan profile obtained by interpolating such 125 values is compared to the A-scan delivered by using the conventional FT based OCT method using three approaches: FFT only, re-sampling using linear interpolation before FFT, and re-sampling using cubic spline interpolation before FFT. The FWHM of the A-scan peak due to the mirror object define the axial resolution of each method.

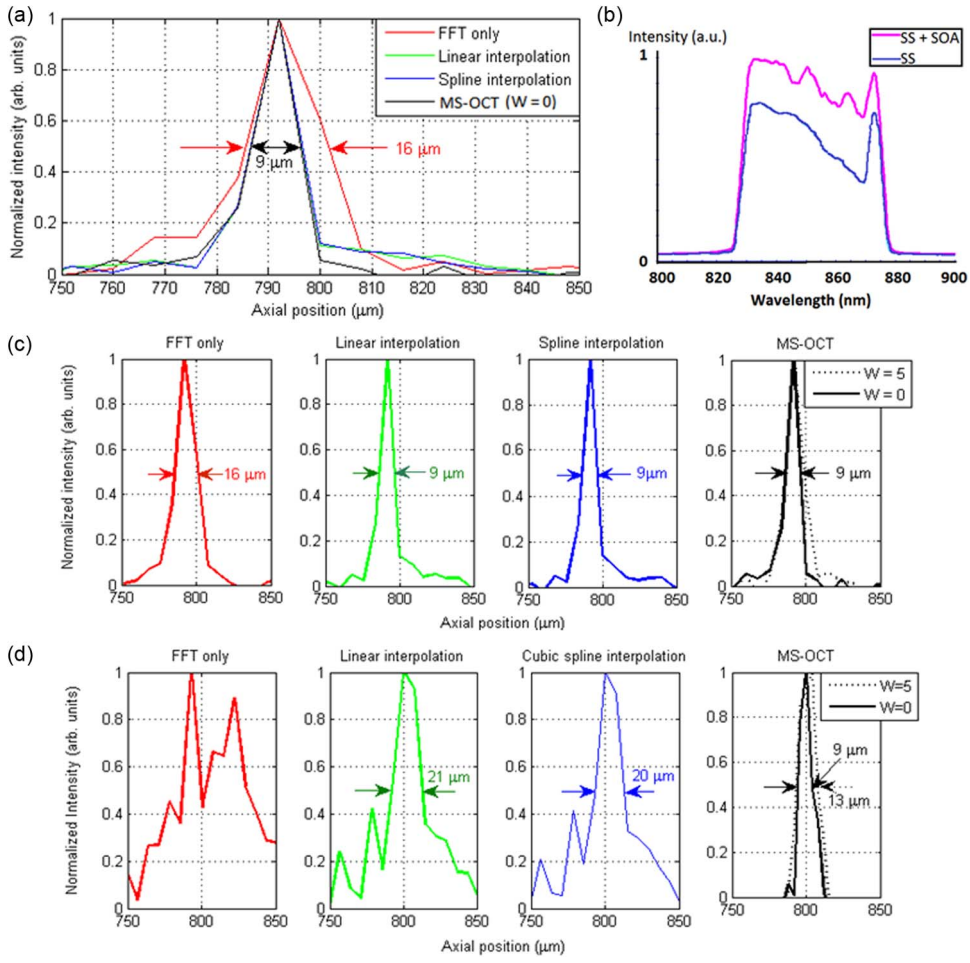

Fig. 4. (a) Normalized A-scan data with a linear scale measured from a single reflector at $z = 592$ μm, using the FT-OCT method without re-sampling (red), with re-sampling via linear interpolation (green), with re-sampling via cubic spline interpolation (blue), and using MS-OCT method with two W values: $W = 0$ (solid black) and $W = 5$ (dotted black). (b) Measured spectra of the swept source output (purple line) and at the output of the optical amplifier (blue line). (c) Normalized A-scan plots in linear scale, showing the FWHM width as a quantification of the axial resolution of each method investigated. (d) Same as in (c), when the DE [in Fig. 1(a)] is inserted in the reference path.

The normalized A-scan profiles are shown superposed in Fig. 4(a) and side-by-side in Fig. 4(c). With FFT only (red), the A-scan presents a poor axial resolution characterized by a FWHM of 16 μm. By re-sampling data via linear interpolation (green) and cubic spline interpolation (blue) before FFT, the FWHM improves to $\sim$9 μm.

The FWHM of the A-scan peak produced by the MS-OCT method reaches a similar value of 9 μm to that of the peaks obtained with FFT after spectrum re-sampling, [extreme right graphs in Fig. 4(c)]. As mentioned above, to cover for phase variations between the times the masks have been collected until they are used, it is desirable to increase the window value W. This, however, is at the expense of axial resolution [14], [16], as shown in Fig. 4(c) on extreme right panel, where the A-scan peaks are represented comparatively for $W = 0$ (solid line) and $W = 5$ (dotted black line).

The axial resolution improvement from 16 μm to 9 μm as a result of applying spectrum re-sampling indicates the presence of spectrum chirping, which is a compound effect of nonlinear sweeping and interferometer dispersion due to the thickness of the beam-splitter BS in Fig. 1(a). Channeled spectrum chirping distorts the shape of the A-scan, leading to a smaller amplitude

and a wider peak. Wavenumber re-sampling is necessary to enhance both sensitivity and axial resolution if the conventional FT based method is used. In contrast, 9 μm is measured from the MS-OCT A-scan, similar to the value obtained with the FT-OCT method with re-sampling. This confirms that MS-OCT is immune to the spectrum chirp. The A-scans of MS-OCT with $W = 0$ and $W = 5$ present similar shapes.

Since the central wavelength of the swept source is 850 nm and its tuning range 45 nm, for a Gaussian spectrum shape, a theoretical depth resolution of 7.1 μm [22] should be obtained. All measured values of our A-scans are however larger than this theoretical value. The reason for this discrepancy may be due to the non-Gaussian shape of the tuning spectrum shown in Fig. 4(b), which exhibits several narrow peaks. To demonstrate the tolerance to dispersion of the MS-OCT, we inserted a dispersive element, a slab of glass tube of 25.4 mm thick (DE in Fig. 1) into the reference arm of the interferometer and repeated the measurements of the A-scan signal from the OM. The re-sampling index for FT-OCT was updated for the heavily chirped spectrum data. The measured A-scans are shown in Fig. 4(d). The A-scan (red line) for FT-OCT without re-sampling spreads into two peaks. With re-sampling, linear interpolation (green line) and cubic spline interpolation (blue line), the A-scan profile regains the approximate shape of a single peak, however with some secondary peaks and a FWHM of the main peak of 21 μm for linear interpolation and 20 μm for cubic spline interpolation, wider than the values obtained without the DE. Better correction is achieved by using the MS-OCT method, where using the minimum window size, $W = 0$ (solid black line), the value of the FWHM of 9 μm obtained without the DE is re-obtained. For a larger window size, $W = 5$ (dotted black line), the FWHM becomes wider, reaching 13 μm, however still significantly better than the values achieved by using either of the re-sampling procedures before FFT. Fewer secondary peaks are exhibited by the MS graphs. This demonstrates the tolerance of the MS method to dispersion, in agreement with the results presented in [23] for a flying spot implementation of the MS method.

4. Sensitivity of Master–Slave Full-Field Swept Source OCT

Sensitivity and signal-to-noise ratio (SNR) values of FT-OCT and MS-OCT are evaluated employing a similar target to that used in the previous experiment, a neutral-density (ND) filter of optical density (OD) 2.0 in front of a mirror OM. To further reduce saturation of the camera due to utilization of the mirror, the camera was run at 60K fps. No booster was used, i.e., the power delivered to the OM was 1.5 mW. For the FT-OCT method, the sensitivity is calculated using

$$\text{Sensitivity}_{\text{FT}} = 40 + 20\log\left[\frac{S_{\text{FT}}(\text{OPD}_{\text{peak}})}{\sigma_{\text{FT}}}\right] \tag{3}$$

where $S_{\text{FT}}(\text{OPD}_{\text{peak}})$ denotes the amplitude of the A-scan peak, located at OPD_{peak}, and σ_{FT} signifies the rms noise value measured around the axial position of the A-scan with the OM removed. Forty dB are added to compensate for the attenuation introduced by the ND filter, which transforms SNR calculations here into sensitivity evaluations according to the procedure described in [14]. Similarly, for the MS-OCT method, the sensitivity is defined by

$$\text{Sensitivity}_{\text{MS}} = 40 + 20\log\left[\frac{S_{\text{MS}}(\text{OPD}_p)}{\sigma_{\text{MS}}(\text{OPD}_p)}\right] \tag{4}$$

where $S_{MS}(OPD_p)$ stands for the value obtained by the MS-OCT algorithm applied for the OM placed at an OPD_p and $\sigma_{MS}(OPD_p)$ is the rms value of the correlation between the mask and the spectra acquired with the OM removed.

Sensitivity values were measured with the OM at 6 axial locations from 200 μm to 1.2 mm with a 200 μm increment. Using the FT-OCT method, the A-scan were calculated twice using the same spectra data, with and without *k*-linearization. These results are compared to those obtained by processing the same data using the MS-OCT method, as shown in Fig. 5. The error bars indicate the standard deviation of results evaluated over five sample groups of data, acquired in 10 hours at 2-hour intervals. As shown in Fig. 5, the curve produced using FT-OCT

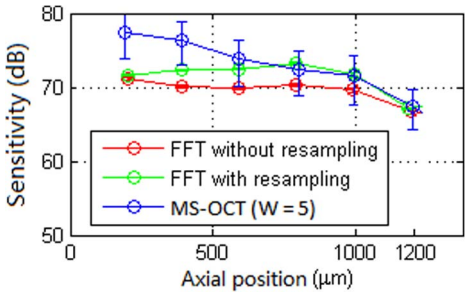

Fig. 5. Sensitivity with error bars versus axial position of the OM, i.e., z, measured from $z = 200$ μm to 1.2 mm in 200 μm increments. (Red line) FT-OCT method without re-sampling. (Green line) FT-OCT method with re-sampling. (Blue line) MS-OCT $(W = 5)$ method.

with resampled channeled spectrum data (green line) exhibits some enhancement over that produced using the original channeled spectrum data (red line) for most of the axial range, apart from 1.2 mm. The maximum sensitivity for FT-OCT is 71.7 dB at $z = 0.2$ mm with a 6 dB roll-off at $\sim$1.2 mm. The Sensitivity (z) profile for the MS-OCT method displays slightly better values than those of the FT-OCT for $z < 0.7$ mm. The maximum sensitivity for MS-OCT $(W = 5)$ is 76.9 dB at $z = 0.2$ mm, with a 6 dB roll-off at $\sim$1.0 mm.

A comparison can be made in terms of sensitivity with the scanning SS-OCT systems published before using a swept source [14], [16]. For the results in Fig. 4, the images were acquired at a 60k fps, that leads to a 16 μs integration. This is slightly longer than the integration time in [14] and [16], evaluated as the inverse of the tuning rate of 100 kHz used. In [14], [16], sensitivity of 95 dB was achieved using FFT based method and 99 dB using the MS method. The sensitivity of the setup presented here is 22–23 dB less than that in the scanning set-up. Considering the 1.5 mW used to illuminate the sample covering 1024 $\times$ 1024 pixels, a power of 1.44 nW per pixel on average is much smaller than that used in the scanning configuration, 2.2 mW in [14] and [16] (although at a longer wavelength). These results should be compared with those reported in [20], using an ultrafast 2-D camera (on a similar wavelength, similar swept source), where a similar sensitivity of 72 dB was reported using an integration time of 9.7 μs and 92 nW per pixel. The camera used here is however slower than that in [20], which means that the noise characteristics of the two cameras are different and a perfect comparison between our set-up and that in [20] is not possible. Similar sensitivity was obtained for a power per pixel approximately 64 times smaller but with an integration time approximately 1.6 times larger. In terms of comparing a scanning SS-OCT setup with a full-field SS-OCT setup, both based on a FFT conventional protocol, the discussion in [24] presents differences between the two configurations, that impact on the performance of imaging. The main difference refers to less confocality of full-field configurations in comparison with scanning configurations that leads to cross talk from lateral pixels in full-field configurations. This aspect is equally valid to MS implementations of scanning and full-field solutions. However, what MS may bring to full-field solutions, is compensation for their lower sensitivity based on better dispersion compensation as well as on enhancement of SNR due to averaging over the window W. Another difference is that of the power sent to the sample. The report suggests that power to the sample can be increased by a factor of 67 when using full field illumination (specifically for the eye imaging), allowing further increase in sensitivity. A MS full-field implementation can also take advantage of such a possible improvement.

To evaluate mask stability over a long period of time, we have performed 3 acquisitions, each including five repetitive measurements at two axial locations: $z = 400$ μm and $z = 1600$ μm. These two locations are selected to evaluate the system stability at small OPD and large OPD values respectively. The first group of data (a) was acquired immediately after the two MCSs were acquired; the second group (b) was acquired 1 hour after and the third group (c) was acquired after 7 days. The SNR, the signal intensity and errors of the measurements are plotted in Fig. 6. We can see that there is little change of both the SNR and signal intensity in 1 hour. After

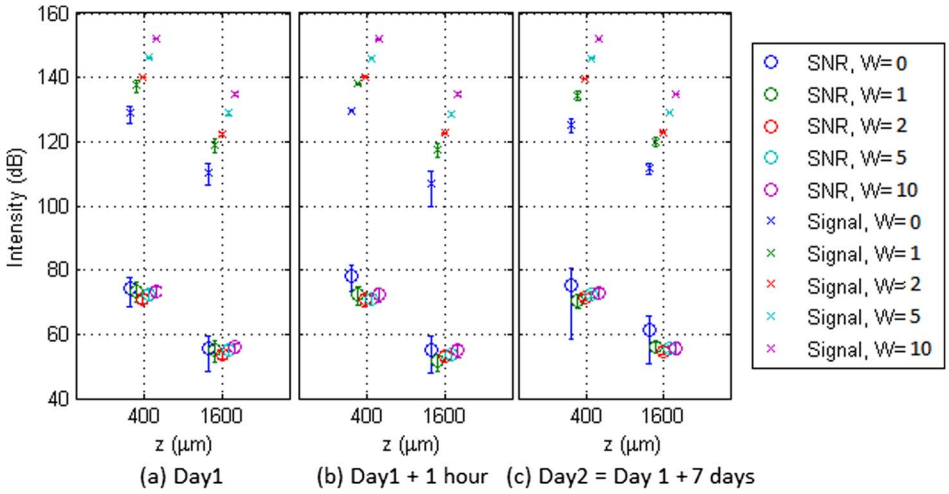

Fig. 6. SNR (circles) and signal intensity (crosses) of MS interferometry measurements from a 40 dB attenuated mirror placed at two axial positions: $z = 400$ μm and $z = 1600$ μm measured at (a) a few seconds, (b) 1 hour, and (c) 7 days after the master channeled spectra were acquired. Five different values of $W = 0$, 1, 2, 5, and 10 were used.

a week, the error of SNR when using $W = 0$ increases two to three times, as expected, due to phase shifts between the MCS and the component with the same modulation period within the SCS; however, the error when using any W larger than 1 changes insignificantly.

5. Computing Speed

The computer used in our experiments employs a 2.67 GHz Intel Xeon X5650 CPU with 6 GB RAM. MATLAB running on Windows 7 is used as the platform to compare the processing time required by the MS-OCT method and by the FT-OCT method. All computing times are calculated by averaging 100 000 clocked operations in both regimes, FT-OCT and MS-OCT. A 16-bit FFT of a channeled spectrum of $N = 500$ data points, requires $t_{FT} = 36.7 \pm 0.33$ μs. However, if spectrum re-sampling is needed, the linear interpolation increases the time to $t_{FT} = 242 \pm 19.8$ μs and the cubic spline algorithm to $t_{FT} = 1100 \pm 71.7$ μs, considering a single correction, based on the phase evaluated at a single optical path difference only. Multiple phase corrections, for multiple optical path differences would obviously require longer. The linear interpolation combined with FFT performs four times faster than the cubic spline interpolation combined with FFT; however, the cubic spline algorithm produces better sensitivity decay with depth and better axial resolution, as documented in [25]. A single cross-correlation takes $t_{MS} = 278.0 \pm 31.0$ μs, however, by applying a short correlation algorithm customized to the MS method [16], the processing time for a single calculation with $W = 0$ can be reduced to $t_{MS} = 26.0 \pm 3$ μs, which is shorter than any FT-OCT algorithm; with $W = 5$, the processing time increases to $t_{MS} = 367 \pm 15$ μs, which is shorter than the time for a single FFT step with cubic spline interpolation but is longer than that using the linear interpolation. For example, in order to produce an *en face* image of 512 $\times$ 128 pixels using the FT-OCT method, 65 536 channeled spectra need to be resampled and Fourier transformed to deliver the same number of A-scans, which requires 65.5 s using the cubic-spline interpolation or 15.9 s using the linear interpolation. This, however, does not include the time to software cut the volume to deliver the *en face* slice. In comparison, the MS-OCT based on the short correlation algorithm [15] required 1.7 s for $W = 0$ and 24.1 s for $W = 5$ with no need of software cutting to deliver an *en face* OCT image of 512 $\times$ 128 pixels. This shows that MS-OCT can perform faster than FT-OCT if small W values are used, and it is comparable in speed with the FFT based methods when large values of W are employed. MS-OCT can become the method of choice if the swept source is highly nonlinear, which would demand an even better linearization than that employed here. In highly

nonlinear cases, the linear interpolation fails, and therefore, a cubic spline algorithm is required. Even more refined linearization methods are needed if the interferometer is not compensated for dispersion, which would further increase the computing time. In the calculation of times required by the FT-OCT case above, correction was done based on phase acquired from a single optical path difference only. The presence of high order dispersion may even require re-sampling the same spectrum data using phase information from more than one axial position to obtain an A-scan corrected evenly in all axial space. This requires an even longer time than the values presented here as examples for the FT-OCT. In contrast, the MS-OCT method is tolerant to dispersion and can deliver *en face* images quicker than the FT-OCT method when the re-sampling via linear interpolation is insufficient to correct the spectrum data. Utilization of graphic card units (GPU)s [25] can reduce the processing time of both methods, by performing the computing processes in parallel, leading ideally to a time required for only one FFT step t_{FT} (for the FT-OCT method) or for only one correlation step t_{MS} (for the MS method).

6. *In vivo en face* Imaging

To test the imaging performance of MS-OCT on scattering samples, a *Drosophila melanogaster* fly in its larval stage was used as the target (see OBJ in Fig. 1). *In vivo en face* images were created using the MS-OCT method and the conventional FT-OCT with spectrum re-sampling from the same image sequence. A 20 μs integration time was used on the camera in the image acquisition. Considering the maximum depth of 2.00 mm, 250 images obtained by FT-OCT are separated by 8.00 μm; therefore, when performing MS-OCT, the MCSs were recorded with an 8 μm increment from $z = 0$ to $z = 1$ mm. The *en face* images acquired from the *Drosophila* flies at their larval (a and b) and pupal stage (c and d) at various depths using FT-OCT (a and c) and MS-OCT (b and d) are presented side by side in Fig. 7. The images exhibit similar features at either stage. At the larval stage, the body of the fly is more reflective than it is at pupal stage, therefore most signal acquired in the images comes from the body surface though some body wall musculature can still be observed. In the pupa stage, the body is more scattering and static, this allows observing some internal structures, labeled with red arrows in Fig. 7(c) and (d) underneath the fly body surface (labeled with yellow arrows).

More *en face* images were acquired *in vivo* from the finger skin of one of the authors, using the FT-OCT and the MS-OCT. A 20 μs exposure time was used in this experiment. Several *en face* images acquired using both methods are shown in Fig. 8, together with reconstructed B-scan images from the 3-D volume obtained using FT-OCT. In the *en face* images, two sweat ducts can be observed at 288 μm, 376 μm, and 400 μm according to the morphology described in [26] marked by yellow arrows in Fig. 8. The structure of the observed sweat glands can be confirmed by reconstructed B-scan images at corresponding locations, labeled in *en face* images by yellow and red dotted lines respectively. The B-scan images are cut from the 3-D volume across the $x-z$ plane. The sweat duct labeled by red arrows is at an axial location that is close to the focal plane of L3 and, therefore, presents higher transverse resolution and higher intensity in the *en face* images than the one labeled by the yellow arrow. In the B-scans, another sweat duct from a 376 μm depth is identified as illustrated by the yellow arrow. This second sweat duct is situated a bit further from the focal plane of L3 than the first one, and therefore, its *en face* images are slightly blurred, and its intensity in the B-scan images is weaker. Two *en face* images from 376 μm and 400 μm and two B-scan images from two adjacent y positions are displayed to confirm its presence.

7. Conclusion

We demonstrate here a new approach for *en face* OCT imaging employing MS interferometry in a full-field setup. Compared to a scanning OCT scheme, full-field OCT replaces mechanical transverse scanning and sequential signal acquisition with flood-illumination and parallel detection, respectively. As a spectral domain method is used, no mechanical axial scanning is needed either. Compared to a conventional swept source OCT method [20], MS-OCT does not

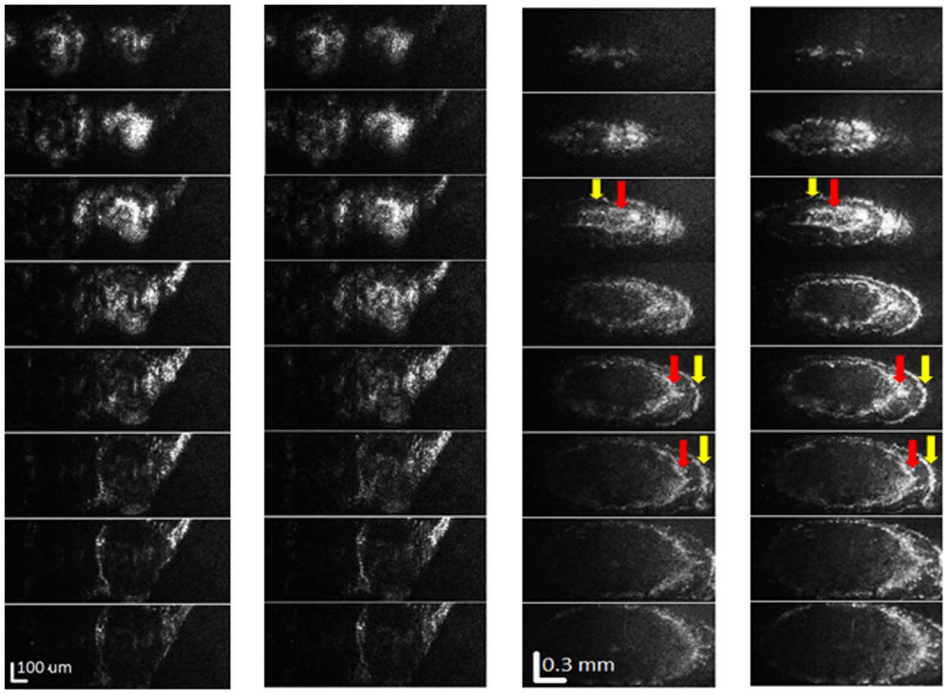

Fig. 7. (a) and (b) *En face* images acquired from a *Drosophila* larva using the FT-OCT (a) and MS-OCT (b); the images in both columns were acquired from eight consecutive depths from the top of the sample, starting from 40 μm to 96 μm with a 8 μm increment from top to bottom. (c) and (d) *En face* images acquired from the *Drosophila* fly at pupa stage using FT-OCT (c) and MS-OCT (d); the images in both columns were acquired from eight depths measured from the top of the sample: 16 μm, 40 μm, 64 μm, 88 μm, 112 μm, 136 μm, 160 μm, and 184 μm, respectively.

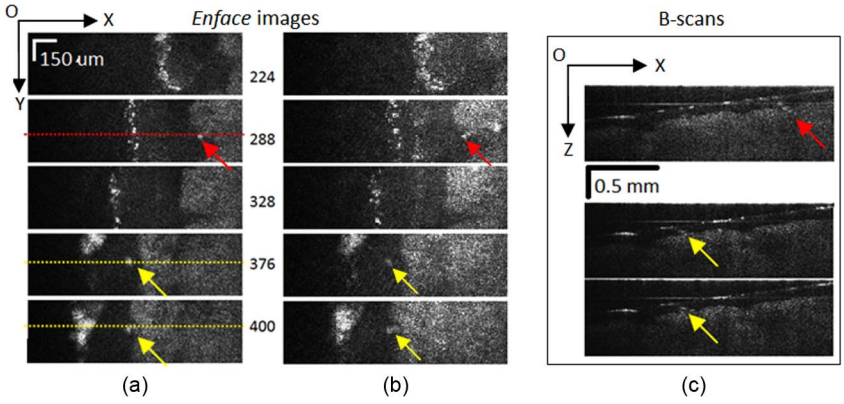

Fig. 8. *En face* images generated using the FT-OCT (a) and MS-OCT (b) method from finger skin, from five depths at 224 μm, 288 μm, 328 μm, 376 μm, and 400 μm. Sweat glands are marked by yellow and red arrows and displayed in the B-scan images (c) obtained by software cutting the 3-D volume of assembled A-scans across the $x-z$ plane.

need spectrum re-sampling, while retaining the high sensitivity of a SD-OCT method. The acquisition of masks is needed once only, as long as the tuning characteristic of the swept source and the dispersion component in the system are stable in time. In our study, masks were used over several months with no need of updating. With no need of spectrum re-sampling, the MS method may encourage development of lower cost swept sources, with no attention paid to their tuning linearity, or with no need for a clock. The clock block in the swept source represents an

expensive part of the swept source, and its design based on a Mach–Zehnder interferometer and a fast photodetector, places an additional limit on the maximum axial range. Not needing a clock would lead to lower costs and wider axial range in SS-OCT.

Since reflectivity of scattering centers within the 3-D volume of the tissue can be recovered using the same algorithm, regardless of the axial position or the lateral position, the MS-OCT method is highly suitable to parallel computing algorithms. All points of the image volume are produced by comparing the acquired SCS for each of the lateral pixels with the masks M_p for all depths, p. The depth is determined by the mask M_p while the set of $SCS_{x,y}$ for all (x, y) pixels maps the output to all transverse locations, which allows all signal processing to be performed in parallel channels. This obviously requires a large number of processing units, thus GPU cards or field programmable gate array (FPGA) processors are more suitable solutions than central processing unit (CPU) processors. Potentially, a parallel computing strategy based on GPUs and CUDA or FPGA presents the potential to reduce the time to produce an *en face* image or a 3-D OCT volume to the time to infer a single interference data point. The main simplification brought here by the MS method consists in eliminating the need to split the A-scan in its multiple depth resolved parts (as required by the FT-OCT method) when interference due to a certain depth alone is needed. The MS method can be harnessed to deliver depth resolved information along different hardware lines in parallel.

The tolerance to dispersion of the MS method is demonstrated by introducing a glass slab in one of the interferometer arms. In such situations, even if the swept source is linear in its sweep, linearization is required when applying the FT-OCT method, that increases the computing time. Compensation of dispersion increases the cost of the interferometer, introduces extra stray reflections and some losses. The MS method can tolerate such dispersion for no penalty in either the computing time, the axial resolution or the decay with depth profile.

The full-field swept source MS-OCT method can be easily implemented on any existing full-field OCT system driven by a swept source and controlled by a conventional FFT protocol. To implement the MS-OCT protocol on such a system, no hardware alteration is required, as long as the system is equipped with a micrometer translation stage that can be employed to assist acquiring the masks. Once the masks are acquired and stored, the MS-OCT program can be installed and dual functionality can be achieved, via the existing FFT conventional route, to produce A-scans or via the MS route, to deliver the reflectivity from several depths simultaneously.

The method presented is ideally suited to FPGA equipped cameras in portable devices to produce an *en face* image direct. The main problem for FFT based systems is the need of collecting the whole volume of data and transferring all such data for processing to a PC. This requires cameras with large memory space on board and a fast digital interface to output the data. However, if a single *en face* OCT image is needed, a single correlator is required for the MS-OCT method to process the whole volume of data and a single image is output from the camera. As commented in Section 4, generally, full-field solutions deliver smaller sensitivity than scanning solutions. The slight sensitivity enhancement, of 4–5 dB achievable via increasing the window W may help in making the full-field implementations competitive with respect to their scanning counterparts by using the MS method.

Acknowledgements

The authors wish to thank the anonymous reviewers for their valuable suggestions. They also thank P. Phelan, Cell Biology, Cancer Targets, and Therapies Group, School of Biosciences, University of Kent, for providing them with *Drosophila* larvae and pupae.

References

[1] J. F. De Boer *et al.,* "Improved signal-to-noise ratio in spectral-domain compared with time-domain optical coherence tomography," *Opt. Lett.*, vol. 28, no. 21, pp. 2067–2069, Nov. 2003.

[2] R. Leitgeb *et al.,* "Spectral measurement of absorption by spectroscopic frequency-domain optical coherence tomography," *Opt. Lett.*, vol. 25, no. 11, pp. 820–822, Jun. 2000.

[3] M. Choma, M. Sarunic, C. Yang, and J. Izatt, "Sensitivity advantage of swept source and Fourier domain optical coherence tomography," *Opt. Exp.*, vol. 11, no. 18, pp. 2183–2189, Sep. 2003.
[4] A. G. Podoleanu, G. M. Dobre, and D. A. Jackson, "En-face coherence imaging using galvanometer scanner modulation," *Opt. Lett.*, vol. 23, no. 3, pp. 147–149, Feb. 1998.
[5] S. Jiao, R. Knighton, X. Huang, G. Gregori, and C. Puliafito, "Simultaneous acquisition of sectional and fundus ophthalmic images with spectral-domain optical coherence tomography," *Opt. Exp.*, vol. 13, no. 2, pp. 444–452, Jan. 2005.
[6] S. Jiao, C. Wu, R. W. Knighton, G. Gregori, and C. A. Puliafito, "Registration of high-density cross sectional images to the fundus image in spectral-domain ophthalmic optical coherence tomography," *Opt. Exp.*, vol. 14, no. 8, pp. 3368–3376, Apr. 2006.
[7] S. H. Yun, C. Boudoux, G. J. Tearney, and B. E. Bouma, "High-speed wavelength-swept semiconductor laser with a polygon-scanner-based wavelength filter," *Opt. Lett.*, vol. 28, no. 20, pp. 1981–1983, Oct. 2003.
[8] R. Tripathi, N. Nassif, J. S. Nelson, B. H. Park, and J. F. de Boer, "Spectral shaping for non-Gaussian source spectra in optical coherence tomography," *Opt. Lett.*, vol. 27, no. 6, pp. 406–408, Mar. 2002.
[9] N. Nassif *et al.,* "In vivo high-resolution video-rate spectral-domain optical coherence tomography of the human retina and optic nerve," *Opt. Exp.*, vol. 12, no. 3, pp. 367–376, Feb. 2004.
[10] Z. Hu and A. M. Rollins, "Fourier domain optical coherence tomography with a linear-in-wavenumber spectrometer," *Opt. Lett.*, vol. 32, no. 24, pp. 3525–3527, Dec. 2007.
[11] J. Xi, L. Huo, J. Li, and X. Li, "Generic real-time uniform k-space sampling method for high-speed swept-source optical coherence tomography," *Opt. Exp.*, vol. 18, no. 9, pp. 9511–9517, Apr. 2010.
[12] B. Potsaid *et al.,* "Ultrahigh speed 1050 nm swept source/Fourier domain OCT retinal and anterior segment imaging at 100,000 to 400,000 axial scans per second," *Opt. Exp.*, vol. 18, no. 19, pp. 20 029–20 048, Apr. 2010.
[13] Y. Yasuno *et al.,* "Three-dimensional and high-speed swept-source optical coherence tomography for in vivo investigation of human anterior eye segments," *Opt. Exp.*, vol. 13, no. 26, pp. 10 652–10 664, Dec. 2005.
[14] A. G. Podoleanu and A. Bradu, "Master–slave interferometry for parallel spectral domain interferometry sensing and versatile 3D optical coherence tomography," *Opt. Exp.*, vol. 21, no. 16, pp. 19 324–19 338, Aug. 2013.
[15] A. Bradu and A. G. Podoleanu, "Calibration-free B-scan images produced by master/slave optical coherence tomography," *Opt. Lett.*, vol. 39, no. 3, pp. 450–453, Feb. 2014.
[16] A. Bradu and A. G. Podoleanu, "Imaging the eye fundus with real-time en-face spectral domain optical coherence tomography," *Biomed. Opt. Exp.*, vol. 5, no. 4, pp. 1233–1249, Apr. 2014.
[17] B. R. Biedermann *et al.,* "Real time en face Fourier-domain optical coherence tomography with direct hardware frequency demodulation," *Opt. Lett.*, vol. 33, no. 21, pp. 2556–2558, Nov. 2008.
[18] A. Dubois, L. Vabre, A.-C. Boccara, and E. Beaurepaire, "High-resolution full-field optical coherence tomography with a Linnik microscope," *Appl. Opt.*, vol. 41, no. 4, pp. 805–812, Feb. 2002.
[19] J. Wang, M. Hathaway, V. Shidlovski, C. Dainty, and A. Podoleanu, "Evaluation of the signal noise ratio enhancement of SS-OCT versus TD-OCT using a full field interferometer," *Proc. SPIE*, 2009, vol. 7168, pp. 71–6. [Online]. Available: http://dx.doi.org/10.1117/12.809043
[20] T. Bonin, G. Franke, M. Hagen-Eggert, P. Koch, and G. Httmann, "In vivo Fourier-domain full-field OCT of the human retina with 1.5 million a-lines/s," *Opt. Lett.*, vol. 35, no. 20, pp. 3432–3434, Oct. 2010.
[21] G. Hausler and M. W. Lindner, "Coherence radar and spectral radar—New tools for dermatological diagnosis," *J. Biomed. Opt.*, vol. 3, no. 1, pp. 21–31, Jan. 1998.
[22] E. A. Swanson *et al.,* "High-speed optical coherence domain reflectometry," *Opt. Lett.*, vol. 17, no. 2, pp. 151–153, Jan. 1992.
[23] A. Bradu, M. Maria, and A. G. Podoleanu, "Demonstration of tolerance to dispersion of master/slave interferometry," *Opt. Exp.*, vol. 23, no. 11, pp. 14 148–14 161, Jun. 2015.
[24] T. Bonin, P. Koch, and G. Httmann, "Comparison of fast swept source full-field OCT with conventional scanning OCT," in *Proc. SPIE*, 2011, pp. 1–8. [Online]. Available: http://dx.doi.org/10.1117/12.889630
[25] S. Van der Jeught, A. Bradu, and A. G. Podoleanu, "Real-time resampling in Fourier domain optical coherence tomography using a graphics processing unit," *J. Biomed. Opt.*, vol. 15, no. 3, pp. 1–3, May/Jun. 2010.
[26] M. Ohmi, M. Tanigawa, Y. Wada, and M. Haruna, "Dynamic analysis for mental sweating of a group of eccrine sweat glands on a human fingertip by optical coherence tomography," *Skin Res. Technol.*, vol. 18, no. 3, pp. 378–383, Aug. 2012.